ADVANCED FUNCTIONAL MATERIALS
www.afm-journal.de

Materials Views
www.MaterialsViews.com

Large Upconversion Enhancement in the "Islands" Au–Ag Alloy/$NaYF_4$: Yb^{3+}, Tm^{3+}/Er^{3+} Composite Films, and Fingerprint Identification

Xu Chen, Wen Xu, Lihang Zhang, Xue Bai, Shaobo Cui, Donglei Zhou, Ze Yin, Hongwei Song,* and Dong-Hwan Kim*

The surface plasmon (SP) modulation is a promised way to highly improve the strength of upconversion luminescence (UCL) and expand its applications. In this work, the "islands" Au–Ag alloy film is prepared by an organic removal template method and explored to improve the UCL of $NaYF_4$: Yb3+, Tm^{3+}/Er^{3+}. After the optimization of Au–Ag molar ratio ($Au_{1.25}$–$Ag_{0.625}$) and the size of $NaYF_4$ nanoparticles (NPs, ≈7 nm), an optimum enhancement as high as 180 folds is obtained (by reflection measurement) for the overall UCL intensity of Tm^{3+}. Systematic studies indicate that the UCL enhancement factor (EF) increases with the increased size of metal NPs and the increase of diffuse reflection, with the decreased size of $NaYF_4$ NPs, with the decreased power density of excitation light and with improving order of multiphoton populating. The total decay rate varies only ranging of about 20% while EF changes significantly. All the facts above indicate that the UCL enhancement mainly originates from coupling of SP with the excitation electromagnetic field. Furthermore, the fingerprint identification based on SP-enhanced UCL is realized in the metal/UC system, which provides a novel insight for the application of the metal/UC device.

1. Introduction

Rare-earth (RE)-doped upconversion nanophosphors (UCNPs) are currently attracting considerable interests owing to their application potential in the fields of in vivo fluorescence imaging,[1–3] biosensing,[4,5] infrared photodynamical therapeutics,[6–8] infrared detection,[9] anticounterfeiting,[10–12] fingerprint identification,[13] solar cells,[14–16] and etc. However, due to lower upconversion luminescence (UCL) efficiency and smaller excitation cross-sections for the 4*f*–4*f* transitions of RE-doped UCNPs, the practical applications have been largely limited.[17] For instance, the non-damage irradiation threshold of the infrared light around 980 nm is less than 4 W cm^{-2} for in vivo application,[18,19] and the total power density of solar spectrum, which distributes widely in the ultraviolet, visible, near-infrared and mid-infrared region, is only ≈100 mW cm^{-2}.[20] Actually, the UCNPs can hardly satisfy with these requirements, therefore it is imminent to enhance the luminescent strength/efficiency of UCNPs. Up to now, various methods, such as the controlling of size, structure, and surface of UCNPs,[14,21,22] the choosing of optimum host matrices and RE dopants,[23–27] the design of core–shell structure[2,28,29] and organic antenna,[30] and the modulation of surface plasmon[5,31,32] have been widely explored to enhance the UCL signals.

Plasmonic modulation by the noble metal NPs has been considered as an effective method to largely improve the luminescent strength of UCNPs.[33–35] As well known, plasmonic nanostructures can concentrate the incoming light into strong localized electric fields (*E*) distributed within the subwavelength regions close to the surface of the nanostructures (≈2–10 nm), leading to the near-field enhancement approaching to two orders of magnitude.[31,36,37] Theoretically, the emission intensity of traditional photoluminescent materials such as quantum dots, dyes, and lanthanide-based phosphors satisfies the linear relationship with the square of the electric field intensity ($|E|^2$), while the UCL intensity is proportional to the 2*n*-th power of the electric field intensity ($|E|^{2n}$ for a n-photon UC process).[38,39] So it is expected that more significant enhancement induced by plasmonic modulation can be obtained in UCNPs, especially for those high-order multi-photon UCL processes. In previous literatures, various gold or silver nanostructures have been utilized to amplify the UCL signals of the well-known $NaYF_4$: Yb^{3+}, Tm^{3+} (Er^{3+}) UCNPs, and the enhancement factor of the overall UCL strength usually varies from several to several ten times, which is much lower than the theoretical prediction.[31,40] It should be highlighted that Chou and co-workers[41] recently prepared a periodic structure of gold by the nanoimprint technique, on which the overall UCL intensity of $NaYF_4$: Yb^{3+}, Er^{3+}

Dr. X. Chen, Dr. W. Xu, Dr. L. H. Zhang, Dr. X. Bai, Dr. D. L. Zhou, Dr. Z. Yin, Prof. H. W. Song
State Key Laboratory on Integrated Optoelectronics
College of Electronic Science and Engineering
Jilin University
2699 Qianjin Street, Changchun 130012, P. R. China
E-mail: wen_xu09@163.com; songhw@jlu.edu.cn
Dr. W. Xu, Prof. D.-H. Kim
School of Chemical and Biomedical Engineering
Nanyang Technological University
70 Nanyang Drive, 637457 Singapore
Dr. S. B. Cui
College of Physics
Jilin University
2699 Qianjin Street, Changchun 130012, P. R. China

DOI: 10.1002/adfm.201502419

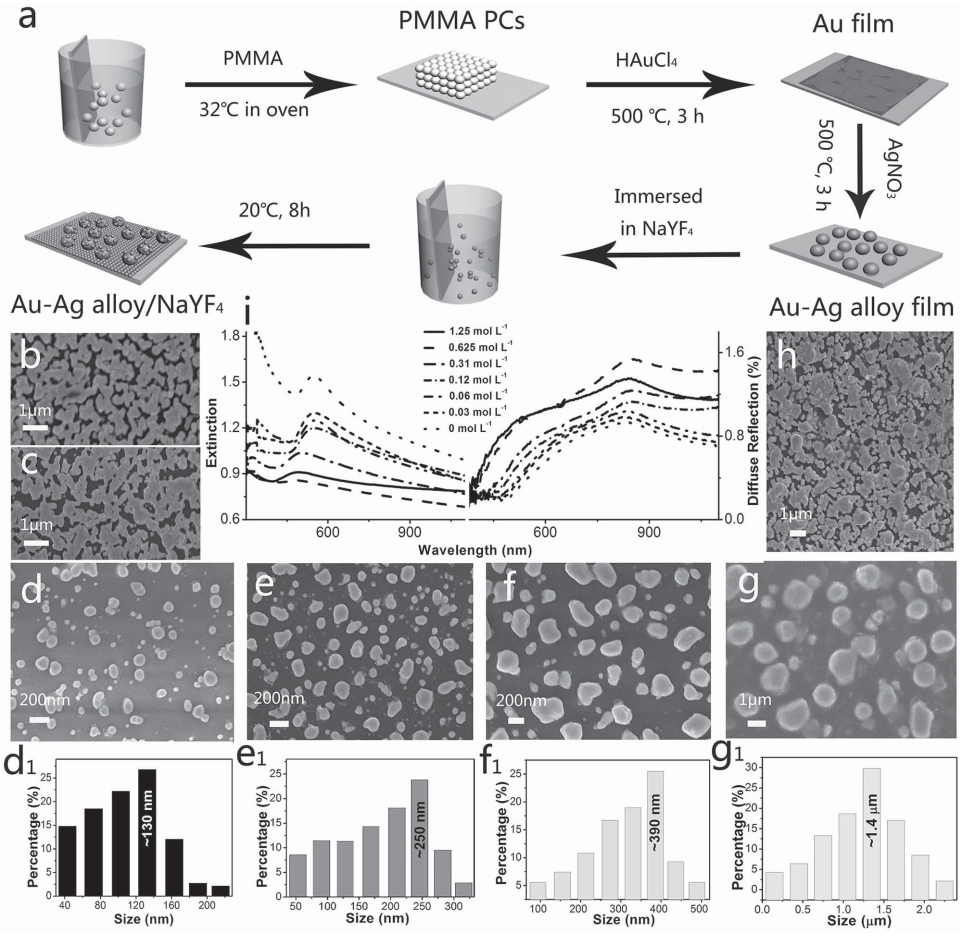

Figure 1. a) Schematic illustrations of the porous Au–Ag/$NaYF_4$: Yb^{3+}, Tm^{3+} composite film formation process. b–h) SEM images of $Au_{1.25}$–Ag_x alloy films with different $AgNO_3$ solution concentration of b) 0, c) 0.03, d) 0.06, e) 0.12, f) 0.31, g) 0.625, and h) 1.25 mol L^{-1}. d_1–g_1) Histogram of the particle size distributions correlated with the SEM of d–g) from several overview SEM images. i) The extinction (left) and diffuse reflection (right) spectra of different $Au_{1.25}$–Ag_x (x = 0–1.25 mol L^{-1}) alloy films.

was improved more than 100 times. However, the equipment for preparing the structure is expensive and complicated, thus the result is difficult to be popularized.

Au–Ag alloy nanostructure is a possible candidate for achieving more significant, repeatable, and stable UCL modulation in comparison to pure silver and gold nanostructures. First, Au–Ag alloy structure could realize higher near-field amplification due to the electronic field coupling between Au and Ag.[42,43] Second, although pure Ag has higher extinction cross-section, the excellent plasmonic property of Ag nanostructures has not been fully utilized in practical applications because of their poor chemical and structural stabilities. The Au–Ag alloy structure can combine higher stability of Au and higher extinction cross-section of Ag.[44] Third, the heterogeneous structure is helpful of generating islands and preventing interparticle agglomerations[45,46] and thus improving the ratio of scattering cross-section to absorption cross section.[47] Very recently, Fang and co-workers[42] reported the randomly aggregated hollow Au–Ag alloy nanourchins enhanced Raman scattering, in which the maximum enhancement factor reached nine orders of magnitude. It should be highlighted that until now the UCL enhancement based on the modulation of Au–Ag alloy nanostructure was rarely reported.

Here, we present a stable, reproducible "islands" Au–Ag alloy film structure prepared by a simple organic self-assembly and template removal method, which demonstrates super-broad surface plasmon resonance (SPR) band extending to 1100 nm. Through the coupling between $NaYF_4$: Yb^{3+}, Tm^{3+} UCNPs, and SPR of Au–Ag alloy nanostructure, repeatable and stable UCL enhancement as high as ≈180 fold was obtained. The application of the Au–Ag/$NaYF_4$: Yb^{3+}, Tm^{3+}/Er^{3+} composite films for fingerprint identification was also demonstrated, as a typical technological exhibition.

2. Results and Discussion

The Au–Ag alloy film and Au–Ag/$NaYF_4$: 20% Yb^{3+}, 0.2% Tm^{3+} composites were prepared by a poly(methylmethacrylate) (PMMA) opal template removal method and the synthesis schematic is shown in the flowchart of **Figure 1**a. The adoption of organic template and removal by heat treatment can ensure the formation of island structure for the Au–Ag alloy film and the separation of alloy particles, which is significant for shortening the interaction distance between Au–Ag alloy film and

the $NaYF_4$: Yb^{3+}, Tm^{3+} UCNPs, and enhancing the coupling of SPR with the UCNPs.[34] In order to further increase the coupling with SPR, the average size of $NaYF_4$: Yb^{3+}, Tm^{3+} UCNPs dispersed onto Au–Ag alloy film was controlled ranging of 7–50 nm (see Figure S1, Supporting Information). Figure 1b–h show the scanning electron microscopy (SEM) images of pure Au film and various Au–Ag alloy films as the concentration of $HAuCl_4$ is fixed at 1.25 mol L^{-1}. It is obvious that when the concentration of $AgNO_3$ is lower (0–0.03 mol L^{-1}), the morphologies of Au–Ag alloy films are similar to that of the pure Au film, in which the agglomeration of particles occurs and there is no clear boundary among the metal particles. As the concentration of $AgNO_3$ increases from 0.03 to 0.625 mol L^{-1}, clear boundaries among Au–Ag alloy particles are identified and a large number of large "islands" occur. The Au–Ag alloy film is composed of the randomly distributed and irregular Au–Ag particles without aggregation, ranging of 130 nm to 1.4 μm (see Figure $1d_1$–g_1). While the concentration of $AgNO_3$ further increases to 1.25 mol L^{-1}, the Au–Ag alloy film changes to relatively dense film like as the pure Au film. The extinction spectra (left) and diffused reflectance spectra (right) of SPR for the $Au_{1.25}$–Ag_x alloy films are as shown in Figure 1i. The broadbands extending of 350–1100 nm are distinguished in all the Au–Ag alloy films, which show that the surface plasmon extinction (SPE) of Au–Ag alloy films arise from the contributions of both the transverse and longitudinal modes of localized SP owing to the irregular shapes of Au–Ag alloy films and strong plasmon coupling among the neighboring Au–Ag alloy NPs.[34,42] This phenomenon allows the SP of Au–Ag films coupling with either the 980 nm excitation light or the emission lines of $NaYF_4$: Yb^{3+}, Tm^{3+}. It is interesting to observe that as the concentration of $AgNO_3$ increases, the SPE peaks show a gradual blue shift from original location of 530 nm. The transverse SPR of Ag NPs is about 400 nm, while that of Au NPs is around 530 nm, with the increase of Ag concentration, the contribution of Ag SPR increases, leading to the blue-shift of SPR in the alloy composites.[44] With the concentration of $AgNO_3$ increasing from 0 to 0.625 mol L^{-1}, the extinction decreases obviously, along with the Au–Ag alloy film changing from the relatively dense film to the porous film. The separated Ag–Au NPs increase and enlarge, resulting in the decrease of absorption and the increase of scattering in the same time. As the concentration of $AgNO_3$ exceeds 0.625 mol L^{-1}, the extinction increases along with the Au–Ag alloy film changing from the porous film to the dense film again. And as the concentration of $AgNO_3$ reaches to 0.625 mol L^{-1}, the extinction is the lowest. In the diffuse reflectance spectra, two SPR bands are identified. The weaker one locates around 500 nm (it also blue shifts with the increase of Ag concentration), while the stronger one centers around 850 nm. This indicates that the longitude SPR modes contribute dominantly to the diffuse reflection. The intensity change of the 850 nm band in the diffuse reflectance spectra is exactly opposite to the visible extinction band. For Au–Ag composite film prepared with 0.625 mol L^{-1} $AgNO_3$, the diffuse reflectance around 850 nm is the strongest. The reflectance spectra were also measured (see Figure S3, Supporting Information), which shows that the reflectance ranging of 350–1100 nm was only about 4% for all the samples, which should have rare influence on the UCL enhancement. It should be noted that with the forming of the porous Au–Ag film, the clear boundaries among metal particles can be identified, which is helpful of improving the ratio of scattering to absorption cross-section and restraining the thermal loss of the excitation light.[46]

In order to identify the formation of Au–Ag alloy films and Au–Ag/$NaYF_4$: Yb^{3+}, Tm^{3+} composite film further, they were scraped from the glass substrate and dispersed in ethanol, then dropped onto the copper grids for high-resolution transmission electron microscopy (HRTEM) measurements and energy-dispersive X-ray analysis (EDX). **Figure 2**a–c display the TEM image and EDX elemental mappings of Au–Ag alloy NPs, respectively. It can be distinguished that the elements of Au and Ag distribute homogeneously in the sample. The EDX analysis further indicates the formation of Au–Ag alloy NPs (Figure 2d). The X-ray power diffraction (XRD) patterns and the typical HR-TEM image of the pure Au film, Au–Ag alloy film and Ag film are shown in Figure 2e and the inset. No obvious difference among different samples is identified due to the same crystalline structure and close lattice constants for cubic Au and Ag. Furthermore, the SEM images of Au–Ag/$NaYF_4$: Yb^{3+}, Tm^{3+} composite film are shown in Figure 2f. It is known that the $NaYF_4$: Yb^{3+}, Tm^{3+} UCNPs (≈20 nm) are evaporated into the pores and on the surface of the Au–Ag alloy NPs, indicating the formation of Au–Ag/$NaYF_4$: Yb^{3+}, Tm^{3+} composite film. In order to further determine the structure of the porous composite film, a HR-TEM image of $NaYF_4$: Yb^{3+}, Tm^{3+} on the surface of an Au–Ag alloy particle is shown in Figure 2g. It is apparent that the Au–Ag alloy NP is surrounded by a number of $NaYF_4$: Yb^{3+}, Tm^{3+} UCNPs, forming a dense, solitary $NaYF_4$: Yb^{3+}, Tm^{3+} layer on the surface of the Au–Ag alloy NP, driven by surface tension of the liquid in the evaporating process. This kind of structure can effectively shorten the interaction distance between the UCNPs and the alloy NPs and is helpful of UCL enhancement.[33]

The density of $NaYF_4$: Yb^{3+}, Tm^{3+} UCNPs on the alloy film has great impact on the strength of UCL. It should be noted that in the preparation of composite and reference samples, we deposited the same size, the same concentration, and the same quantity of UCNPs on the glass (reference sample) and the Au–Ag alloy film. Judged from this fact, the average density of $NaYF_4$ Yb^{3+}, Tm^{3+} between the composites and reference samples should be the same. In order to prove this point further, the extinction of UCNPs on the glass and the Au–Ag/$NaYF_4$: Yb^{3+}, Tm^{3+} were calculated and compared through measuring the transmission by an integrating sphere (see Figure S4, Supporting Information). The results show that the average density of $NaYF_4$: Yb^{3+}, Tm^{3+} UCNPs in the reference and composite samples is nearly the same (see S2.4 and Table S1, Supporting Information).

The SP modulation of the Au–Ag alloy film on the UCL of $NaYF_4$: Yb^{3+}, Tm^{3+} NPs under 980 nm excitation was systemically studied. In the following text, the UCL was all measured and compared through the reflection measurement (RM) and the schematic of the optical paths for the measurement is shown on the top of **Figure 3**. Note that the optical paths have great influence on the result of UCL enhancement. Furthermore, the UCL enhancement was also measured by an integrating sphere, which showed that for the optimum

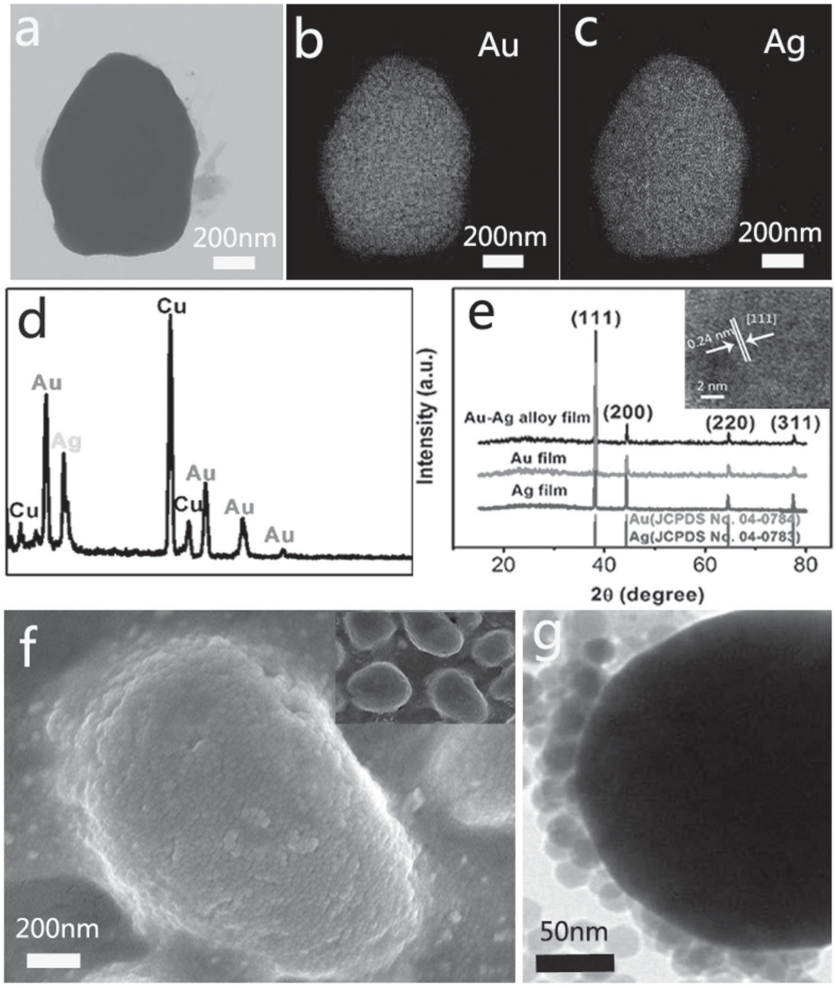

Figure 2. Energy-dispersive X-ray (EDX) mappings of Au–Ag alloy film at the top of the figure a) alloy, b) Au, c) Ag. d) EDX analysis of Au–Ag alloy. e) XRD patterns of the pure Au film, Au–Ag alloy film, and Ag film, and the typical HR-TEM image of Au–Ag alloy film in inset. f) SEM images of Au–Ag/$NaYF_4$: Yb^{3+}, Tm^{3+} composite film. g) TEM image of $NaYF_4$: Yb^{3+}, Tm^{3+} on the surface of an Au–Ag alloy particle.

Au–Ag/$NaYF_4$: Yb^{3+}, Tm^{3+} composite film, an EF of ≈124 fold could be obtained (see Figure S5, Supporting Information). EFs obtained in the integrating sphere were about 70% of those obtained by the RM. This indicate that the EF enhancement mainly originate from the SPR effect, rather than simple optical effect. A schematic illustration on the UC populating and emission processes of $NaYF_4$: Yb^{3+}, Tm^{3+} under 980 nm excitation and the corresponding UCL spectra are shown in Figure 3a, b, respectively. Yb^{3+} and Tm^{3+} pairs demonstrate typical energy transfer (ET) UCL, Yb^{3+} ions taken as absorbers and Tm^{3+} ions as activators. The UC emissions span from ultraviolet to near-infrared, populating from two-step until to five-step ET, as reported in previous literatures (see Figure 3a).[48] In Figure 3b, there exhibit intense multiple emissions of Tm^{3+} ions, assigned to the transitions of $^1I_6$–$^3F_4$ at 346 nm (five-photon), $^1D_2$–$^3H_6$ at 361 nm and $^1D_2$–$^3F_4$ at 451 nm (four-photon), $^1G_4$–$^3H_6$ at 475 nm and $^1G_4$–$^3F_4$ at 648 nm (three-photon), $^3F_2$–$^3H_6$ at 696 nm, $^3F_3$–$^3H_6$ at 726 nm and $^3H_4$–$^3H_6$ at 800 nm (two-photon), respectively. For comparison, EF is defined, as the ratio of UCL intensity of the metal/$NaYF_4$: Yb^{3+}, Tm^{3+} composite film to that of $NaYF_4$: Yb^{3+}, Tm^{3+} film (reference) measured in the same experimental conditions. Figure 3c presents the EF of Au, Ag, $Au_{0.625}$–Ag_x and $Au_{1.25}$–Ag_x/$NaYF_4$: Yb^{3+}, Tm^{3+} composite films ($NaYF_4$ UCNPs, ≈30 nm) as a function of the $HAuCl_4$ and $AgNO_3$ concentration, respectively. In the pure Au/$NaYF_4$: Yb^{3+}, Tm^{3+} and Ag/$NaYF_4$: Yb^{3+}, Tm^{3+} films, the EFs originally increase with the increase of $HAuCl_4$/$AgNO_3$ concentration, and then are almost the same when the $HAuCl_4$/$AgNO_3$ concentration exceeds 0.625 mol L^{-1}. The optimum EFs are, respectively, approximately ninefold and ≈15 fold for Au/$NaYF_4$: Yb^{3+}, Tm^{3+} and Ag/$NaYF_4$: Yb^{3+}, Tm^{3+} films. In the Au–Ag alloy film (the concentration of $HAuCl_4$ is fixed at 0.625 and 1.25 mol L^{-1}), the EF increases first, and approaches at an optimum as the ratio of Au/Ag equals to 2, then decreases as the ratio of Au/Ag increases further. The optimum EFs are about ≈14 fold and ≈78 fold, for $Au_{0.625}$–Ag_x/$NaYF_4$: Yb^{3+}, Tm^{3+} and $Au_{1.25}$–Ag_x/$NaYF_4$: Yb^{3+}, Tm^{3+} composite films, respectively. Figure 3d demonstrates the dependence of EFs on the extinction (at 980 nm) and the diffuse reflection (at 980 nm) of the composite films, which indicates that EF decreases with the increase of the extinction, while increases with the increase of diffuse reflection. This suggests that the absorption modes of SPR are negative to the UCL enhancement, while the diffraction modes (diffuse reflection) are positive, which is in consistent with the theoretical prediction.[49] It is suggested that the excitation light absorbed by the Au–Ag alloy film can be swiftly transferred to thermal energy, leading to the significant increase of local temperature for $Au_{1.25}$–Ag_x/$NaYF_4$: Yb^{3+}, Tm^{3+} composites. As a consequence, the nonradiative relaxations for Tm^{3+}/Yb^{3+} ions increase, and the UCL of Tm^{3+} quenches. On the contrary, the diffraction of the Au–Ag alloy may improve the availability of $NaYF_4$: Yb^{3+}, Tm^{3+} UCNPs to the excitation light. Figure 3e shows the EF versus the average size of Au–Ag alloy particles corresponding to Figure $1d_1$–g_1, which demonstrates that the EF increases rapidly and linearly with the increasing particle size of Au–Ag alloy NPs. The extinction of a metal NP is due to both absorption and scattering. Considering small spherical particles and particles with a size comparable to the incident wavelength, the extinction with a dielectric constant ε can be given by,

$$C_E = C_A + C_S = k_1 Im(\alpha) + \frac{k_1^4}{6\pi}|\alpha|^2 \quad (1)$$

$$\alpha = 4\pi r^3 \left(\frac{\varepsilon_m - \varepsilon_1}{\varepsilon_m + 2\varepsilon_1} \right) \quad (2)$$

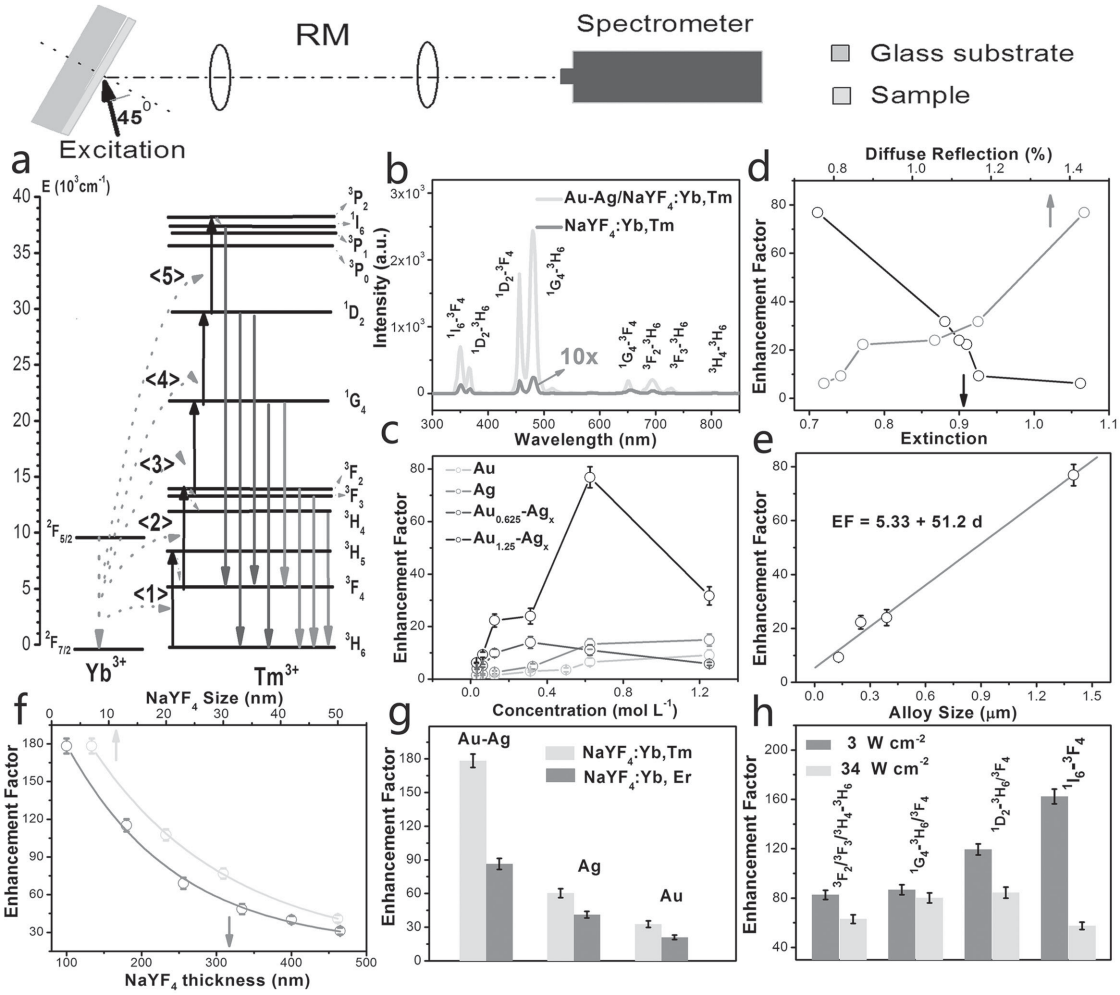

Figure 3. Schematic of the UCL reflection measurement (on the top). a) Schematic of UC populating for $NaYF_4$: Yb^{3+}, Tm^{3+}. b) The UCL spectra of $NaYF_4$: Yb^{3+}, Tm^{3+} (≈7 nm) and Au–Ag/$NaYF_4$: Yb^{3+}, Tm^{3+} films. c) EF of Au, Ag, $Au_{0.625}$–Ag_x, $Au_{1.25}$–Ag_x/$NaYF_4$: Yb^{3+}, Tm^{3+} films versus $HAuCl_4$ and $AgNO_3$ concentration. d) EF versus the diffuse reflection (up) and the extinction (down) in the $Au_{1.25}$–Ag_x/$NaYF_4$: Yb^{3+}, Tm^{3+} films. e) EF versus Au–Ag alloy particle size. f) EF versus $NaYF_4$ particle size and film thickness. The average particle sizes of $NaYF_4$ used in (c–e) are all 30 nm. g) EF of $NaYF_4$: Yb^{3+}, Tm^{3+} /Er^{3+} NPs (≈7 nm) in different composite samples. All the measurements above were performed under 34 W cm^2 980 nm light. h) Dependence of EF of on transitions of $NaYF_4$: Yb^{3+}, Tm^{3+} NPs (30 nm) and excitation power density.

where k_1 is the wavevector of the incident light in medium 1 and α is the polarizability of the sphere of radius r, ε_m is the complex dielectric constant of the metal, ε_1 is the dielectric constant of the medium 1.[49] This shows that the absorption term (C_A) increases as r^3 where the scattering term (C_S) increases as r^6. For this reason, the EF increases largely with the increase of Au–Ag particle size.

The EF of $Au_{1.25}$–$Ag_{0.625}$/$NaYF_4$: Yb^{3+}, Tm^{3+} composite films as a function the size of $NaYF_4$: Yb^{3+}, Tm^{3+} UCNPs and the equivalent thickness of $NaYF_4$: Yb^{3+}, Tm^{3+} film were investigated under the same conditions, as shown in Figure 3f and Figure S6 (Supporting Information) (The thickness of $NaYF_4$: Yb^{3+}, Tm^{3+} on the Au–Ag alloy film cannot be directly determined, because the Au–Ag alloy film is uneven. However, it can be indirectly estimated through that of $NaYF_4$: Yb^{3+}, Tm^{3+} film on the glass, because the average density of $NaYF_4$: Yb^{3+}, Tm^{3+} UCNPs on the glass and on the Au–Ag alloy film is nearly the same). It is apparent that the EF decreases exponentially with the increase of particle size and the equivalent thickness. An optimum EF is obtained (≈180 fold) when ≈7 nm UCNPs is explored to build up the composite film and the film thickness is controlled to be 100 nm. The size-dependent and thickness-dependent behavior can be attributed to the shortness of the interaction distance between Au–Ag alloy NPs and the UCNPs. In general, the field enhancement effect decays exponentially with distance away from the metal surface and the optimum distance or the maximum electric field enhancement are only several nanometers in close proximity of Au–Ag alloy NPs.[31]

A comparison of the optimal EF for $NaYF_4$: Yb^{3+}, Tm^{3+}/Er^{3+} NPs deposited on Au, Ag, and Au–Ag alloy films is shown in Figure 3g, which indicates that the EF for the Au–Ag alloy film is much larger than that of pure Au and Ag films in the same conditions, for both the UCL of Tm^{3+} and Er^{3+} (The detail data on the UCL enhancement of Au–Ag/$NaYF_4$: Yb^{3+}, Er^{3+} UCNPs are shown in Figure S7, Supporting Information). Compared to $NaYF_4$: Yb^{3+}, Er^{3+} UCNPs, the enhancement of

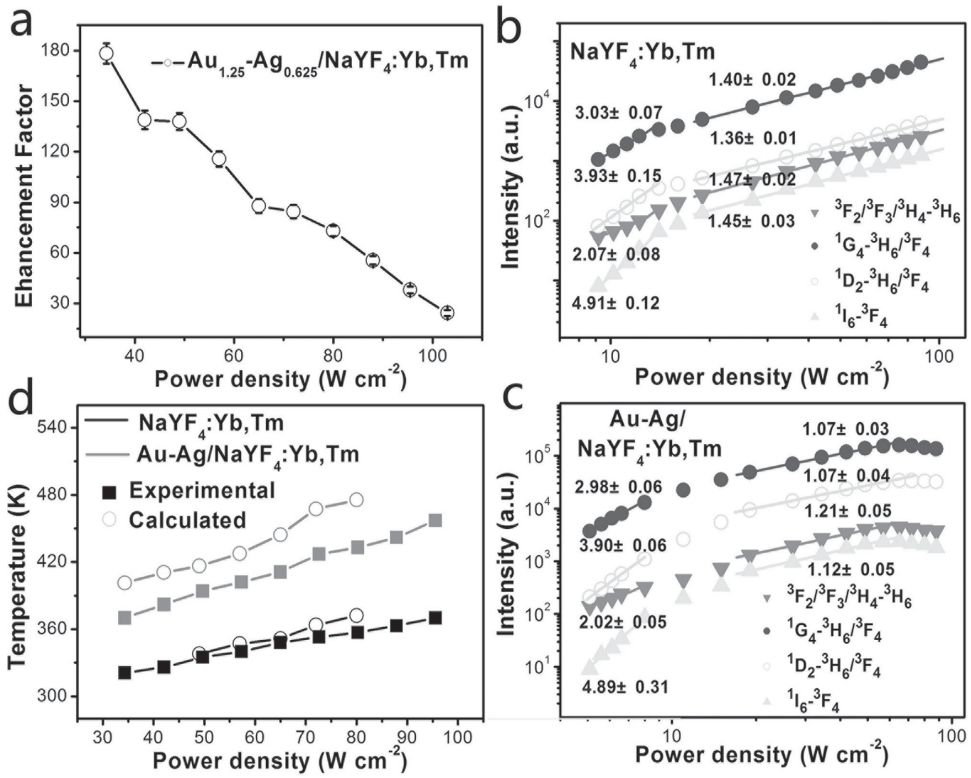

Figure 4. a) The UCL EF as a function of excitation power under 980 nm light excitation. b,c) The power-dependent UCL intensity of different transitions in $NaYF_4$: Yb^{3+}, Tm^{3+} (30 nm) films and Au–Ag/$NaYF_4$: Yb^{3+}, Tm^{3+} composite films. d) The power dependence of temperature in $NaYF_4$: Yb^{3+}, Tm^{3+} films and Au–Ag/$NaYF_4$: Yb^{3+}, Tm^{3+} composite films through the direct measurement (Experimental) and the calculated results (Calculated).

$NaYF_4$: Yb^{3+}, Tm^{3+} UCNPs is more significant, which may be attributed to the contribution of high-order processes in the UCL of $NaYF_4$:Yb^{3+}, Tm^{3+} UCNPs. Basically, in the vicinity of metal NPs, the SPR-induced luminescent enhancement can be classified by the following aspects: 1) the coupling of SPR with the emission electromagnetic field of an emitter, inducing the enhanced radiative rate of the emitter; 2) The coupling of SPR with the excitation field, leading to strength enhancement of local excitation field; 3) The ET between metal NPs and emitters. Our previous studies imply that for the $NaYF_4$: Yb^{3+}, Er^{3+}/Tm^{3+} UCNPs, the UCL enhancement mainly originates from the coupling of SPR with the excitation field.[33] Theoretically, the emission intensity for a multi-photon (n) UCL is proportional to the n-th power of excitation power density (P^n) if the saturation effect and the local thermal effect can be neglected. Thus it is expected that EF increases with the improved order of UCL. Figure 3h shows the transition-dependent UCL enhancement measured at 3 and 34 W cm^{-2} for the Au–Ag/$NaYF_4$: Yb^{3+}, Tm^{3+} composite film consisting of 30 nm UCNPs. It should be highlighted that as the excitation power density is low enough (≈3 W cm^{-2}), the strict photon-dependent upconversion enhancement can be obtained and the EF increases with the increase of the multi-photon process when n changes from two to five. However, when the excitation power density is higher (≈34 W cm^{-2}), the UCL of the five-photon process has a little deviation from this trend, which might be attributed to the influence of saturation effect and local thermal effect. The saturation effect, which induces n deviates from the required photon number, depending on the competition between linear decay and UC processes for the depletion of the intermediate excited states.[38] The local thermal effect originates from the medium absorption and photothermal conversion to excitation light, which leads to the increase of the local temperature of the medium and luminescent quenching.[50] The energy gap from the starting level of the five-photon populating state $^1I_6$ to its nearest down level $^3P_1$ is only 660 cm^{-1}, inducing the easily happening of the nonradiative relaxation of $^1I_6$–$^3P_1$. In the existent of metal NPs, the local temperature of $NaYF_4$: Yb^{3+}, Tm^{3+} can be largely improved in comparison to $NaYF_4$: Yb^{3+}, Tm^{3+} due to large metal SPE at 980 nm and quick thermal transmission from the metal NPs to the UCNPs. Note that for the Au–Ag/$NaYF_4$: Yb^{3+}, Tm^{3+} composite films consisting of other $NaYF_4$: Yb^{3+}, Tm^{3+} NPs (7, 20, and 50 nm), EFs of different transitions have the same variation tendency at the higher excitation power density (≈34 W cm^{-2}, see Figure S8, Supporting Information).

The power-dependent UCL properties are shown in **Figure 4**. From Figure 4a, the EF for the porous $Au_{1.25}$–$Ag_{0.625}$/$NaYF_4$:Yb^{3+},Tm^{3+} (7 nm) composite film gradually decreases from 180 fold to 24 fold as the excitation power increases from 34 to 103 W cm^{-2}. In the existent of metal NPs, the local excitation field is greatly enlarged, resulting in the saturation effect as well as local thermal quenching of UCL and the corresponding suppression of EF with excitation power.[38,50] Figure 4b,c display the double-logarithmic plots of the UCL intensity as a function of excitation power density, for the $NaYF_4$: Yb^{3+}, Tm^{3+} and the porous $Au_{1.25}$–$Ag_{0.625}$/$NaYF_4$: Yb^{3+}, Tm^{3+} composite

films, respectively (the size of UCNPs we used was 30 nm, for both $NaYF_4$: Yb^{3+}, Tm^{3+} film, and the composite film). It should be noted that as the excitation power density is lower than 13 W cm^{-2} for the $NaYF_4$: Yb^{3+}, Tm^{3+} film and lower than 9 W cm^{-2} for the composite film, the slopes of different transitions are near the same to the required photon numbers (n = 2–5) to populate the corresponding levels for $NaYF_4$: Yb^{3+}, Tm^{3+} and Au–Ag/$NaYF_4$: Yb^{3+}, Tm^{3+} films. As the excitation power density ranges of 20–60 W cm^{-2}, the slopes for Au–Ag/$NaYF_4$: Yb^{3+}, Tm^{3+} composite film become smaller than those for $NaYF_4$: Yb^{3+}, Tm^{3+} film, and much smaller than the required photon numbers to populate the corresponding levels. This can be mainly attributed to the saturation effect, and the local thermal effect might also happen in this range. As the excitation power density surpasses 60 W cm^{-2}, the UCL intensities of all the transitions decrease with the further increase of power density. This directly evidenced the happening of thermal quenching effect.

In order to demonstrate the variation of local thermal effect in different samples, the temperature versus excitation power was achieved by two methods (see Figure 4d), the calculated results according to the intensity ratio (R_F) of $^3F_2$–$^3H_6$ to $^3F_3$–$^3H_6$ (see Figure S10, Supporting Information) and the direct measurable data by setting a thermocouple thermometer close to the sample. The data obtained by these two methods are well in consistent. It is obvious that the temperature of the $NaYF_4$: Yb^{3+}, Tm^{3+} film and the Au–Ag/$NaYF_4$: Yb^{3+}, Tm^{3+} composite film both gradually increases with the increasing excitation power, and under the same excitation power the temperature for Au–Ag/$NaYF_4$: Yb^{3+}, Tm^{3+} composite film is higher than that of $NaYF_4$: Yb^{3+}, Tm^{3+} film. This indicates that the photothermal effect of the Au–Ag alloy under 980 nm light excitation have great impact on the variation of EF with excitation power density.

It should be highlighted that in the $Au_{1.25}$–$Ag_{0.625}$/$NaYF_4$:Yb^{3+}, Tm^{3+} composites the threshold power density for generating detectable UCL was measured (see Figure S11, Supporting Information). Relative to the $NaYF_4$:Yb^{3+}, Tm^{3+} film composed of 7 nm UCNPs, the threshold decreases from 34 to 0.2 W cm^{-2}, which is much lower than the non-damage irradiation threshold in vivo application (4 W cm^{-2}) and very close to the total power density of solar spectrum (≈100 mW cm^{-2}). And more, the absolute brightness for the $Au_{1.25}$–$Ag_{0.625}$/$NaYF_4$: Yb^{3+}, Tm^{3+} film (consisting of 7 nm UCNPs, 100 nm in thickness) was measured, to be 127 cd m^{-2} under the excitation of 80 W cm^{-2} 980 nm laser diode, while that for corresponding $NaYF_4$: Yb^{3+}, Tm^{3+} film is too weak to be detected.

In order to further determine the mechanism of UCL enhancement, the decay dynamics of porous Au–Ag/$NaYF_4$: Yb^{3+}, Tm^{3+} composite film, and $NaYF_4$: Yb^{3+}, Tm^{3+} film (≈30 nm) were studied under the excitation of 980 nm pulsed laser. **Figure 5**a shows the UCL decay curves of $^1G_4$–$^3H_6$, $^1D_2$–$^3F_4$, and $^1I_6$–$^3F_4$ transitions in porous $Au_{1.25}$–$Ag_{0.625}$/$NaYF_4$: Yb^{3+}, Tm^{3+} composite films and $NaYF_4$: Yb^{3+}, Tm^{3+} films, respectively, which can be well fitted to the single exponential function. The decay time constants of the $Au_{1.25}$–$Ag_{0.625}$/$NaYF_4$: Yb^{3+}, Tm^{3+} composite film decrease about ≈15% than the pure $NaYF_4$: Yb^{3+}, Tm^{3+} film, for $^1G_4$–$^3H_6$, $^1D_2$–$^3F_4$ and $^1I_6$–$^3F_4$ transitions. Figure 5b–d show the EF and the total decay rate in pure Au, pure Ag, and Ag–Au/$NaYF_4$: Yb^{3+}, Tm^{3+} composite films as a function of the molar concentration of $AgNO_3$ (the molar concentration of pure Au and pure Ag is 1.25 mol L^{-1}). It indicates that while the EF of $^1G_4$–$^3H_6$, $^1D_2$–$^3F_4$, and $^1I_6$–$^3F_4$ transitions changes significantly, the variation of total decay rate changes only ranging of 20%. This fact further indicates that the upconversion enhancement can be mainly attributed to the coupling of SPR with the excitation light, instead of the coupling with the emission light, which alters the radiative transition rate.

To figure out the essence for the variation of the total transition rate, the temperature-dependent nonradiative relaxation rate (W_{NR}) of $^1I_6$–$^3P_1$ was calculated by the multi-photon theory (In the calculation, the phonon energy is chosen as 350 cm^{-1}, corresponding to the phonon threshold of $NaYF_4$: Yb^{3+}, Tm^{3+} UCNPs, see S2.6, Supporting Information). The result demonstrates that as the temperature varies ranging of several 10 °C (see Figure 5e), corresponding to the laser-irradiation induced temperature rising, the variation of W_{NR} is about 20% (Figure 5e inset). This definitely reveals that the variation of the total transition rate (W) in the existent of metal NPs probably originates from the change of W_{NR}, instead of the radiative transition rate for the $^1I_6$–$^3F_4$ transition. Note that the variation of W_{NR} of $^1D_2$–$^1G_4$ and $^1G_4$–$^3F_2$ was also calculated. Considering the energy gaps of $^1D_2$ and $^1G_4$ to their nearest down levels are 6600 and 6200 cm^{-1}, respectively, if we consider only the phonon modes of $NaYF_4$: Yb^{3+}, Tm^{3+} (≈350 cm^{-1}) itself, the multi-phonon relaxations hardly happen. Actually, in the UCNPs, because a large number of surface adsorption bonds such as C—H, C—O, C—C are involved, the nonradiative relaxations of $^1D_2$–$^1G_4$ and $^1G_4$–$^3F_2$ may also happen. We calculated W_{NR} by choosing different phonon modes (2930, 1130, 860 cm^{-1}) based on Fourier transform infrared spectroscopy of $NaYF_4$: Yb^{3+}, Tm^{3+} UCNPs (30 nm) (see Figure S12a, Supporting Information), and the results show that W_{NR} varies largely with phonon modes. In Figure S12b (Supporting Information), the calculation results are given for reference.

In the $NaYF_4$: Yb^{3+}, Tm^{3+} NPs, the inner quantum efficiency of the UCL is very low, and it depends strongly on the particle size of $NaYF_4$: Yb^{3+}, Tm^{3+} (Table S2, Supporting Information). The small variation of the decay time constants in the existent and inexistent of metal NPs indicates that although the UCL is highly improved, the inner quantum efficiency probably has rare change. According to the Beer–Lambert Law (see S2.7, Supporting Information), the absorption coefficient of $NaYF_4$: Yb^{3+} (20%), Tm^{3+} (0.2%) at 980 nm is about 2×10^{-6} nm^{-1}. In the present case, because the film thickness of $NaYF_4$: Yb^{3+}, Tm^{3+} films in $NaYF_4$: Yb^{3+}, Tm^{3+} film and Au–Ag/$NaYF_4$: Yb^{3+}, Tm^{3+} composite film is only about 100 nm (see Figure S6a, Supporting Information), that means, quite a little bit of excitation light (2×10^{-4}) is absorbed by $NaYF_4$: Yb^{3+}, Tm^{3+} film in the absence of metal NPs. We believe that in the presence of metal NPs, the near-field scattering of metal NPs can largely improve the usage of $NaYF_4$: Yb^{3+}, Tm^{3+} to excitation light.

Technically, the plasmon-enhanced UC device is promised to be utilized in various applications. Here, we explored the metal/UC device in high-resolution fingerprint (see **Figure 6**a). In contrast to the other techniques, the fingerprint by the fluorescence of UCNPs can remedy the interference of background from the surface, because the fluorophores in various

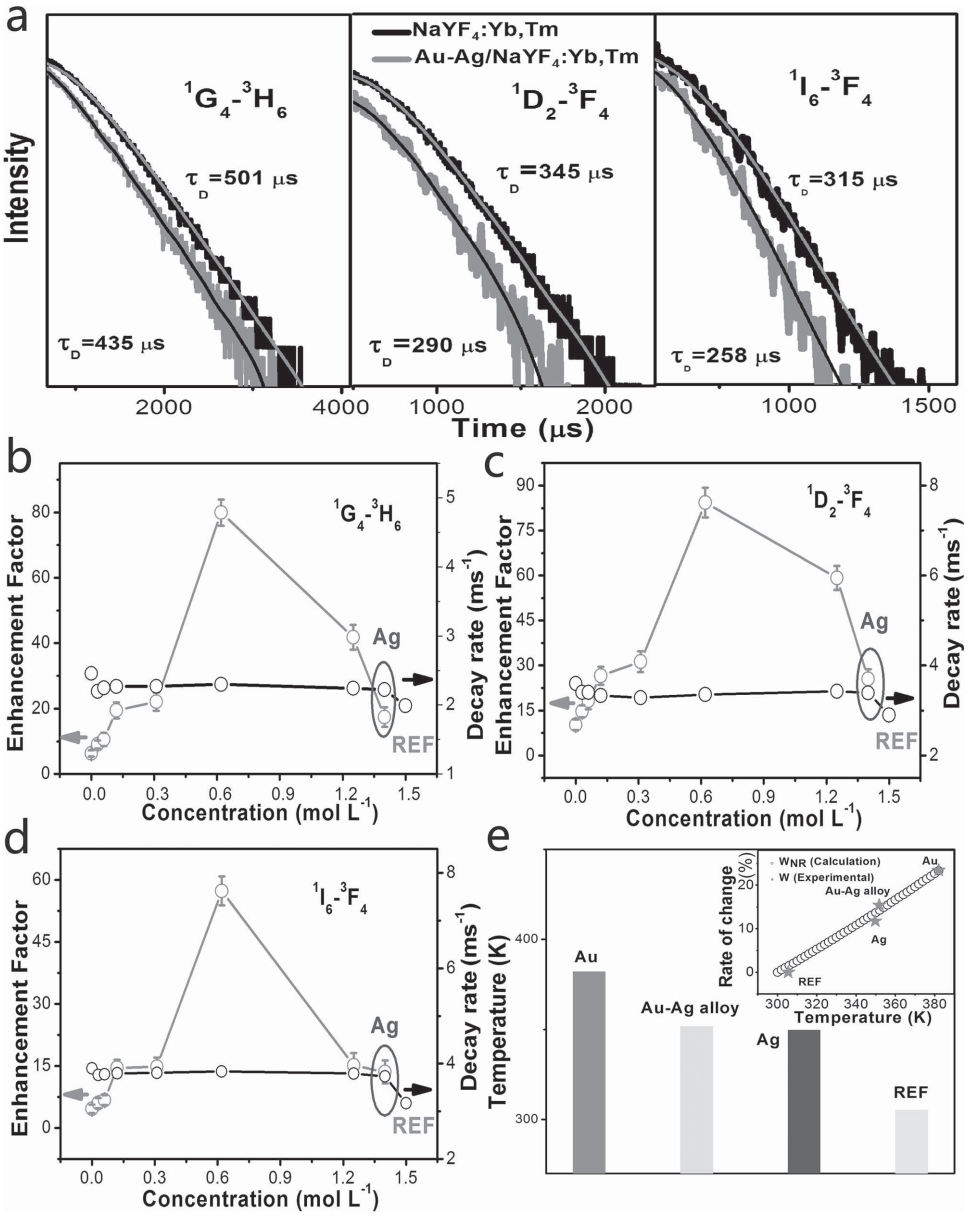

Figure 5. a) The UCL decay curves of different transitions under 980 nm excitation. b–d) The UCL EF and total decay rate of $^1G_4$–$^3H_6$, $^1D_2$–$^3F_4$, and $^1I_6$–$^3F_4$ in Au, Ag, and Au–Ag/$NaYF_4$: Yb^{3+}, Tm^{3+} composite films as a function of the $AgNO_3$ concentration (P_{ex} = 34 W cm^{-2}). e) The deduced sample temperature based on branch ratio of $^3F_2/^3F_3$–$^3H_6$ transitions of the $NaYF_4$: Yb^{3+}, Tm^{3+} (30 nm) film, Au–Ag, Ag, and Au/$NaYF_4$: Yb^{3+}, Tm^{3+} composite film. Inset: the variation of calculated nonradiative relaxation rate (W_{NR}) and the total decay rate (W) of the $NaYF_4$: Yb^{3+}, Tm^{3+} (30 nm) film, Au–Ag, Ag, and Au/$NaYF_4$: Yb^{3+}, Tm^{3+} composite film as a function of the sample temperature.

substrates cannot be excited by near-infrared light, and the imaging of latent fingerprints with UCNPs suffers little from background fluorescence interference, thus offering excellent optical contrast and allowing high detection sensitivity. In addition, UCNPs have excellent properties, such as exceptional photostability, fine-tuned emissions, and long lifetimes, which endow these UCNPs with many advantages over the other fluorescence reagents.[13] Generally to say, the usage of smaller UCNPs in fingerprint can result in higher resolution patterns. However, the brightness of smaller UCNPs is weaker, and the plasmon-enhanced UC device can enhance the brightness of the smaller UCNPs. Figure 6b–e showed the fingerprints obtained by different samples. It can be seen that due to quite weak UCL for the smaller $NaYF_4$: Yb^{3+}, Er^{3+} UCNPs (7 nm), the fingertip pressed directly on the $NaYF_4$: Yb^{3+}, Er^{3+} film/glass substrate is indistinct, dark and without luminescence ridges excited by 980 nm laser light (see Figure 6b). The image exposed on the $NaYF_4$: Yb^{3+}, Er^{3+} film composed of larger UCNPs (≈200 nm) is bright, and the ridge pattern details could be easily recognized (see Figure 6c and c_1), however, the accuracy is poorer. Fortunately, the fingerprint on the Au–Ag/$NaYF_4$: Yb^{3+}, Er^{3+} (≈7 nm) composite films, displays a bright, well-resolved ridge flow and pattern configuration (see Figure 6d,d1). Figure 6e,e1 show the UCL photo of two fingerprints overlapped together

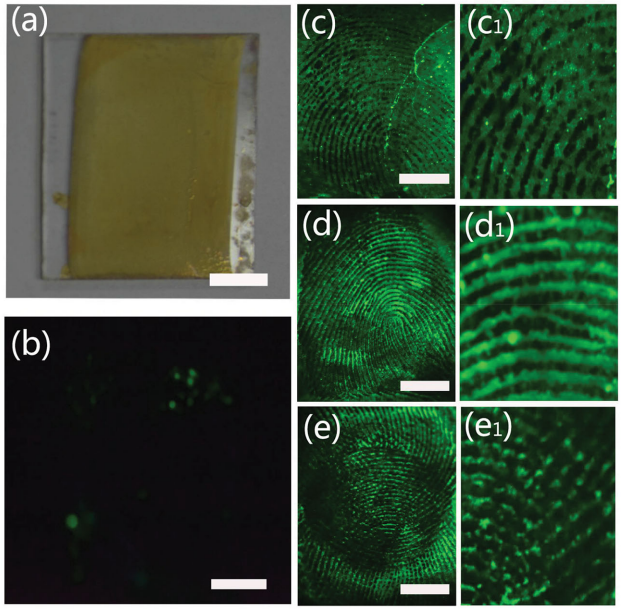

Figure 6. (a) The digital photograph of the $Au_{1.25}$–$Ag_{0.625}$ alloy film. (b) The UCL digital images of a fingerprint on the surface of the glass with $NaYF_4$: Yb^{3+}, Er^{3+} film (≈7 nm). (c),(d) the UCL digital images of a fingerprint on the surface of the glass with $NaYF_4$: Yb^{3+}, Er^{3+} film (≈200 nm) and the Au–Ag/$NaYF_4$: Yb^{3+}, Er^{3+} (≈7 nm) composite film, respectively, and (c_1), (d_1) the corresponding magnified images to c, d. (e) the UCL digital image of two fingerprints overlapped together on the Au–Ag/$NaYF_4$: Yb^{3+}, Er^{3+} NPs (≈7 nm) and (e_1) the corresponding magnified image. The scale bars in all images are 2 mm.

on the Au–Ag/$NaYF_4$: Yb^{3+}, Er^{3+} (≈7 nm) composites. From the high-magnification image, the ridges of two fingerprint crossed in two different directions can be distinguished easily, further implying that the plasmon-enhanced UC device is powerful in high-resolution imaging.

3. Conclusion

In this work, the "islands" Au–Ag alloy composite films were prepared by the simple two-step PMMA template method and employed to enhance the UCL of $NaYF_4$: Yb^{3+}, Tm^{3+} UCNPs. It can be claimed that a typical "islands" Au–Ag alloy film demonstrated separation of metal NPs and the average size of Au–Ag particle was controllable, ranging of hundreds to thousands nanometers. This resulted in the improvement of the scattering to absorption ratio of the porous film and the shortness of the effective interaction distance between metal and UCNPs. Therefore, the UCL EF in the Au–Ag/$NaYF_4$: Yb^{3+}, Tm^{3+} composite film was largely improved, depending strongly on the size of Au/Ag alloy metals and the size of the $NaYF_4$: Yb^{3+}, Tm^{3+} UCNPs. The ≈180-fold enhancement of overall UCL intensity was observed (by RM) in the optimum $Au_{1.25}$–$Ag_{0.625}$/$NaYF_4$: Yb^{3+}, Tm^{3+} composite film. The detailed investigations indicate that the UCL enhancement mainly originates from the coupling of Au–Ag alloys SP with the excitation electromagnetic field of the UCNPs. Furthermore, the high-quality fingerprint identification based on plasmon-enhanced UCL device was realized, which provided a novel insight on the application of metal/UCNPs device system.

4. Experimental Section

Synthesis of the Porous Au–Ag/$NaYF_4$: Yb^{3+}, Tm^{3+} Hybrid Film: The Au–Ag alloy film was produced by the template removal method. First, the colloid suspension (5% solid content) of the PMMA microspheres (260 nm) was dropped onto a glass substrate and placed in a 32 °C oven for 1 d and the spheres were slowly self-organized into highly ordered colloidal arrays on the glass substrate, driven by surface tension of the liquid in the evaporating process. Following deposition, the opals were sintered for 40 min at 120 °C to enhance their physical strength (The photonic stop bands (PSB) of the opals were all around 600 nm). Then, the opals were penetrated with the $HAuCl_4$ solution (a mixed solution of water and ethanol, 1.25 mL L^{-1}). After infiltrated, the resulting products were dried in air at room temperature for 30 min. After that, annealing was carried out with slowly elevated temperature (50 °C h^{-1}) up to 500 °C for 3 h, forming the Au film. Then, the $AgNO_3$ solution with different concentrations was further penetrated on the Au film and the annealing process was repeated, forming the porous Au–Ag alloy film. Finally, the porous Au–Ag film was immersed into $NaYF_4$: Yb^{3+}, Tm^{3+} UCNPs cyclohexane solution (0.02% solid content) with the sizes of 7–50 nm. The $NaYF_4$: Yb^{3+}, Tm^{3+} UCNPs were slowly self-organized into the porous Au–Ag film or on the glass substrate, driven by surface tension of the liquid in the evaporating process.

Characterization: The products were characterized via various routes, such as SEM, TEM, XRD, as well as EDX. To measure the power-dependent UCL spectra, a continuous 980 nm light diode was used to pump the samples. A fluorescence spectrometer (FLS980) of Edinburgh instruments combined with an integrating sphere was used to obtain EF in integrating directions. A Nd:YAG pumping laser, the third-order Harmonic-Generator and a tunable optical parameter oscillator were used to measure the luminescent dynamics.

Supporting Information

Supporting Information is available from the Wiley Online Library or from the author.

Acknowledgements

This work was supported by the Major State Basic Research Development Program of China (973 Program) (no. 2014CB643506), the National Natural Science Foundation of China (Grant nos. 11374127, 11304118, 61204015, 81201738, 81301289, 61177042, and 11174111), the Program for Chang Jiang Scholars and Innovative Research Team in University (no. IRT13018).

Received: June 13, 2015
Published online: August 3, 2015

[1] C. Y. Li, Y. Hou, M. Y. Gao, *Adv. Mater.* **2014**, *26*, 6922.
[2] Y. F. Wang, G. Y. Liu, L. D. Sun, J. W. Xiao, J. C. Zhou, C. H. Yan, *ACS Nano* **2013**, *7*, 7200.
[3] Y. S. Liu, S. Y. Zhou, D. T. Tu, Z. Chen, M. D. Huang, H. M. Zhu, E. Ma, X. Y. Chen, *J. Am. Chem. Soc.* **2012**, *134*, 15083.
[4] L. Y. Wang, R. X. Yan, Z. Y. Huo, L. Wang, J. H. Zeng, J. Bao, X. Wang, Q. Peng, Y. D. Li, *Angew. Chem. Int. Ed.* **2005**, *44*, 6054.
[5] P. Kannan, F. A. Rahim, R. Chen, X. Teng, L. Huang, H. D. Sun, D. H. Kim, *Adv. Mater.* **2012**, *24*, OP236.
[6] S. S. Cui, D. Y. Yin, Y. Q. Chen, Y. F. Di, H. Y. Chen, Y. X. Ma, S. Achilefu, Y. Q. Gu, *ACS Nano* **2013**, *7*, 676.

[7] L. Xia, X. G. Kong, X. M. Liu, L. P. Tu, Y. L. Zhang, Y. L. Chang, K. Liu, D. Z. Shen, H. Y. Zhao, H. Zhang, *Biomaterials* **2014**, *35*, 4146.
[8] P. Huang, W. Zheng, S. Y. Zhou, D. T. Tu, Z. Chen, H. M. Zhu, R. F. Li, E. Ma, M. D. Huang, X. Y. Chen, *Angew. Chem. Int. Ed.* **2014**, *53*, 1252.
[9] M. Kumar, P. Zhang, *Langmuir* **2009**, *25*, 6024.
[10] Y. H. Zhang, L. X. Zhang, R. R. Deng, J. Tian, Y. Zong, D. Y. Jin, X. G. Liu, *J. Am. Chem. Soc.* **2014**, *136*, 4893.
[11] R. Deng, X. Liu, *Nat. Photonics* **2014**, *8*, 10.
[12] Y. Q. Lu, J. B. Zhao, R. Zhang, Y. J. Liu, D. M. Liu, E. M. Goldys, X. S. Yang, P. Xi, A. Sunna, J. Lu, Y. Shi, R. C. Leif, Y. J. Huo, J. Shen, J. A. Piper, J. P. Robinson, D. Y. Jin, *Nat. Photonics* **2014**, *8*, 32.
[13] J. Wang, T. Wei, X. Li, B. Zhang, J. Wang, C. Huang, Q. Yuan, *Angew. Chem. Int. Ed.* **2014**, *53*, 1616.
[14] L. L. Liang, Y. M. Liu, C. H. Bu, K. M. Guo, W. W. Sun, N. Huang, T. Peng, B. Sebo, M. M. Pan, W. Liu, S. S. Guo, X. Z. Zhao, *Adv. Mater.* **2014**, *26*, 5124.
[15] G. B. Shan, G. P. Demopoulos, *Adv. Mater.* **2010**, *22*, 4373.
[16] M. Rudiger, S. Fischer, J. Frank, A. Ivaturi, B. S. Richards, K. W. Kramer, M. Hermle, J. C. Goldschmidt, *Sol. Energy Mater. Sol. Cells* **2014**, *128*, 57.
[17] J. C. Boyer, F. C. J. M. van Veggel, *Nanoscale* **2010**, *2*, 1417.
[18] L. R. Hirsch, R. J. Stafford, J. A. Bankson, S. R. Sershen, B. Rivera, R. E. Price, J. D. Hazle, N. J. Halas, J. L. West, *Proc. Natl. Acad. Sci.* **2003**, *100*, 13549.
[19] Q. Q. Zhan, J. Qian, H. J. Liang, G. Somesfalean, D. Wang, S. L. He, Z. G. Zhang, S. A. Engels, *ACS Nano* **2011**, *5*, 3744.
[20] IEC Standard 60904–3, *Photovoltaic Devices—Part 3: Measurement Principles for Terrestrial Photovoltaic (PV) Solar Devices with Reference Spectral Irradiance Data*, International Electrotechnical Commission, Geneva, Switzerland, http://www.iec.ch (accessed: December 2007).
[21] S. Y. Han, R. R. Deng, X. J. Xie, X. G. Liu, *Angew. Chem. Int. Ed.* **2014**, *53*, 2.
[22] D. Yuan, M. C. Tan, R. E. Riman, G. M. Chow, *J. Phys. Chem. C* **2013**, *117*, 13297.
[23] F. Auzel, *Chem. Rev.* **2004**, *104*, 139.
[24] R. Kumar, M. Nyk, T. Y. Ohulchanskyy, C. A. Flask, P. N. Prasad, *Adv. Funct. Mater.* **2009**, *19*, 853.
[25] J. C. Boyer, L. A. Cuccia, J. A Capobianco, *Nano Lett.* **2007**, *7*, 847.
[26] J. B. Zhao, D. Y. Jin, E. P. Schartner, Y. Q. Lu, Y. J. Liu, A. V. Zvyagin, L. X. Zhang, J. M. Dawes, P. Xi, J. A. Piper, E. M. Goldys, T. M. Monro, *Nat. Nanotechnol.* **2013**, *8*, 729.
[27] R. Martín-Rodríguez, S. Fischer, A. Ivaturi, B. Froehlich, K. W. Kramer, J. C. Goldschmidt, B. S. Richards, A. Meijerink, *Chem. Mater.* **2013**, *25*, 1912.
[28] G. Y. Chen, T. Y. Ohulchanskyy, A. Kachynski, H. Agren, P. N. Prasad, *ACS Nano* **2011**, *5*, 4981.
[29] K. A. Abel, J. C. Boyer, F. C. J. M. van Veggel, *J. Am. Chem. Soc.* **2009**, *131*, 14644.
[30] W. Q. Zou, C. Visser, J. A. Maduro, M. S. Pshenichnikov, J. C. Hummelen, *Nat. Photonics* **2012**, *6*, 560.
[31] M. Saboktakin, X. C. Ye, S. J. Oh, S. H. Hong, A. Fafarman, U. Chettiar, N. Engheta, C. B. Murray, C. R. Kagan, *ACS Nano* **2012**, *6*, 8758.
[32] S. Schietinger, T. Aichele, H. Q. Wang, T. Nann, O. Benson, *Nano Lett.* **2010**, *10*, 134.
[33] M. Saboktakin, X. C. Ye, U. K. Chettiar, N. Engheta, C. B. Murray, C. R. Kagan, *ACS Nano* **2013**, *7*, 7186.
[34] W. Xu, Y. S. Zhu, X. Chen, J. Wang, L. Tao, S. Xu, T. Liu, H. W. Song, *Nano Res.* **2013**, *6*, 795.
[35] S. Fischer, F. Hallermann, T. Eichelkraut, G. V. Plessen, K. W. Krämer, D. Biner, H. Steinkemper, M. Hermle, J. C. Goldschmidt, *Opt. Express* **2013**, *21*, 10606.
[36] C. Ciracì, R. T. Hill, J. J. Mock, Y. Urzhumov, A. I. Fernández-Domínguez, S. A. Maier, J. B. Pendry, A. Chilkoti, D. R. Smith, *Science* **2012**, *337*, 1072.
[37] G. M. Akselrod, C. Argyropoulos, T. B. Hoang, C. Ciracì, C. Fang, J. N. Huang, D. R. Smith, M. H. Mikkelsen, *Nat. Photonics* **2014**, *8*, 835.
[38] M. Pollnau, D. R. Gamelin, S. R. Lüthi, H. U. Güdel, M. P. Hehlen, *Phys. Rev. B* **2000**, *61*, 3337.
[39] J. F. Suyver, A. Aebischer, S. García-Revilla, P. Gerner, H. U. Güdel, *Phys. Rev. B* **2005**, *71*, 125123.
[40] L. Sudheendra, V. Ortalan, S. Dey, N. D. Browning, I. M. Kennedy, *Chem. Mater.* **2011**, *23*, 2987.
[41] W. H. Zhang, F. Ding, S. Y. Chou, *Adv. Mater.* **2012**, *24*, OP236.
[42] Z. Liu, Z. B. Yang, B. Peng, C. Cao, C. Zhang, H. J. You, Q. H. Xiong, Z. Y. Li, J. X. Fang, *Adv. Mater.* **2014**, *26*, 2431.
[43] M. Li, Z. S. Zhang, X. Zhang, K. Y. Li, X. F. Yu, *Opt. Express* **2008**, *16*, 14288.
[44] C. B. Gao, Y. X. Hu, M. S. Wang, M. F. Chi, Y. D. Yin, *J. Am. Chem. Soc.* **2014**, *136*, 7474.
[45] A. Kuzma, M. Weis, M. Daricek, J. Uhrik, F. Horinek, M. Donoval, F. Uherek, D. Donoval, *J. Appl. Phys.* **2014**, *115*, 053517.
[46] D. Gu, C. Zhang, Y. K. Wu, L. J. Guo, *ACS Nano* **2014**, *8*, 10343.
[47] D. D. Evanoff Jr., G. Chumanov, *ChemPhysChem* **2005**, *6*, 1221.
[48] Q. Su, S. Han, X. Xie, H. Zhu, H. Chen, C.-K. Chen, R.-S. Liu, X. Chen, F. Wang, X. Liu, *J. Am. Chem. Soc.* **2012**, *134*, 20849.
[49] J. R. Lakowicz, *Anal. Biochem.* **2005**, *337*, 171.
[50] Q. L. Dai, H. W. Song, X. G. Ren, S. Z. Lu, G. H. Pan, X. Bai, B. Dong, R. F. Qin, X. S. Qu, H. Zhang, *J. Phys. Chem. C* **2008**, *112*, 19694.